Article:
Wang, J.B. and Howe, D. (2004) Design optimization of radially magnetized, iron-cored, tubular permanent-magnet machines and drive systems. IEEE Transactions on Magnetics, 40 (5). pp. 3262-3277. ISSN: 0018-9464

https://doi.org/10.1109/TMAG.2004.833424

Design Optimization of Radially Magnetized, Iron-Cored, Tubular Permanent-Magnet Machines and Drive Systems

Jiabin Wang, *Senior Member, IEEE,* and David Howe

***Abstract*—In this paper we deduce, from analytical field solutions, the influence of leading design parameters on the performance of a radially magnetized, iron-cored, tubular permanent-magnet machine and its drive system. We derive analytical formulas for predicting the open-circuit electromotive force, the thrust force, the iron loss, and the winding resistance and inductances, as well as the converter losses. The force density, the machine and drive system efficiencies, and the power factor and converter volt–ampere (VA) rating are established as functions of a set of machine dimensional ratios, with due account of magnetic saturation and subject to a specified thermal constraint. We validate the utility and accuracy of the analytically derived formulas by finite-element calculations. Finally, we show that the design optimization of such a linear drive system must account for the losses and VA rating of the converter as well as the design parameters of the tubular machine.**

***Index Terms*—Design optimization, electric drive, linear machine, permanent-magnet machine.**

I. Introduction

LINEAR electromagnetic machines, which either convert thrust force directly from a prime mover into electrical energy (e.g., free-piston combustion engine) or provide thrust force directly to a payload (e.g., reciprocating actuator), offer numerous advantages over rotary-to-linear counterparts, notably the absence of mechanical gears and transmission systems, which results in a higher efficiency, higher dynamic performance, and improved reliability. Of the various linear machine topologies, tubular permanent-magnet machines have the highest efficiency, and offer a high power/force density and excellent servo characteristics [1]. Hence, linear permanent-magnet machines are being used increasingly in applications as varied as manufacturing automation [2], electrical power generation [3], transportation [4], healthcare [5], [6], and household appliances [7], [8].

In order to facilitate the design optimization and dynamic modeling of linear permanent-magnet machines, a lumped circuit model is often employed to predict the magnetic field distribution [9], [10]. However, while this allows the relationship between critical design parameters and machine performance to be established analytically, it suffers from problems associated with model inaccuracy, particularly when the leakage flux is significant and the flux paths are complex. Therefore, numerical analysis of the field distribution to facilitate evaluation of performance is also employed [11]–[13]. However, while numerical techniques, such as finite-element analysis, provide an accurate means of determining the field distribution, with due account of saturation, etc., they remain relatively time-consuming and do not provide as much insight as analytical solutions into the influence of the design parameters on the machine behavior. To overcome the aforementioned problems, analytical solutions for the magnetic field distribution in various topologies of linear machine have been established. For example, a single-sided, planar linear permanent-magnet motor has been analyzed using both the magnetic charge image technique [14] and a magnetic vector potential formulation [15], [16].

A general framework and comprehensive analysis and design techniques for slotless tubular permanent-magnet machines have also been reported [17], [18]. However, the force capability of tubular permanent-magnet machines can be improved significantly by employing a slotted armature. Furthermore, the majority of tubular permanent-magnet machines, whether operating as a motor or a generator, are interfaced to an electrical power source via a power electronic converter, whose VA rating, cost, and efficiency are closely related to the performance of the electrical machine. Thus, conventional design techniques, which do not take account of the converter, may lead to a less optimal machine design, and, therefore, a less cost-effective drive system solution. This paper describes analysis and design techniques that have been developed specifically for radially magnetized tubular permanent-magnet machines equipped with a slotted armature. Various performance indicators that are pertinent to their design, such as the open-circuit flux linkage, the thrust force and force ripple, the iron loss, the armature reaction field and the winding inductances, and the demagnetization withstand, etc., are treated within a unified analytical framework. These allow design optimization at a system level, taking account of both the machine and its power electronic converter.

II. Armature Winding Arrangement

The armature of a three-phase tubular permanent-magnet machine can be wound to facilitate either brushless dc or brushless ac operation, as illustrated in Fig. 1.

A. Brushless DC

A brushless dc machine has two coils per pole-pair per phase, displaced 120 electrical degrees apart, as shown in Fig. 1(a).

Manuscript received April 6, 2004; revised June 9, 2004.

The authors are with the Department of Electronic and Electrical Engineering, the University of Sheffield, Sheffield S1 3JD, U.K. (e-mail: j.b.wang@sheffield.ac.uk; d.howe@shef.ac.uk).

Digital Object Identifier 10.1109/TMAG.2004.833424

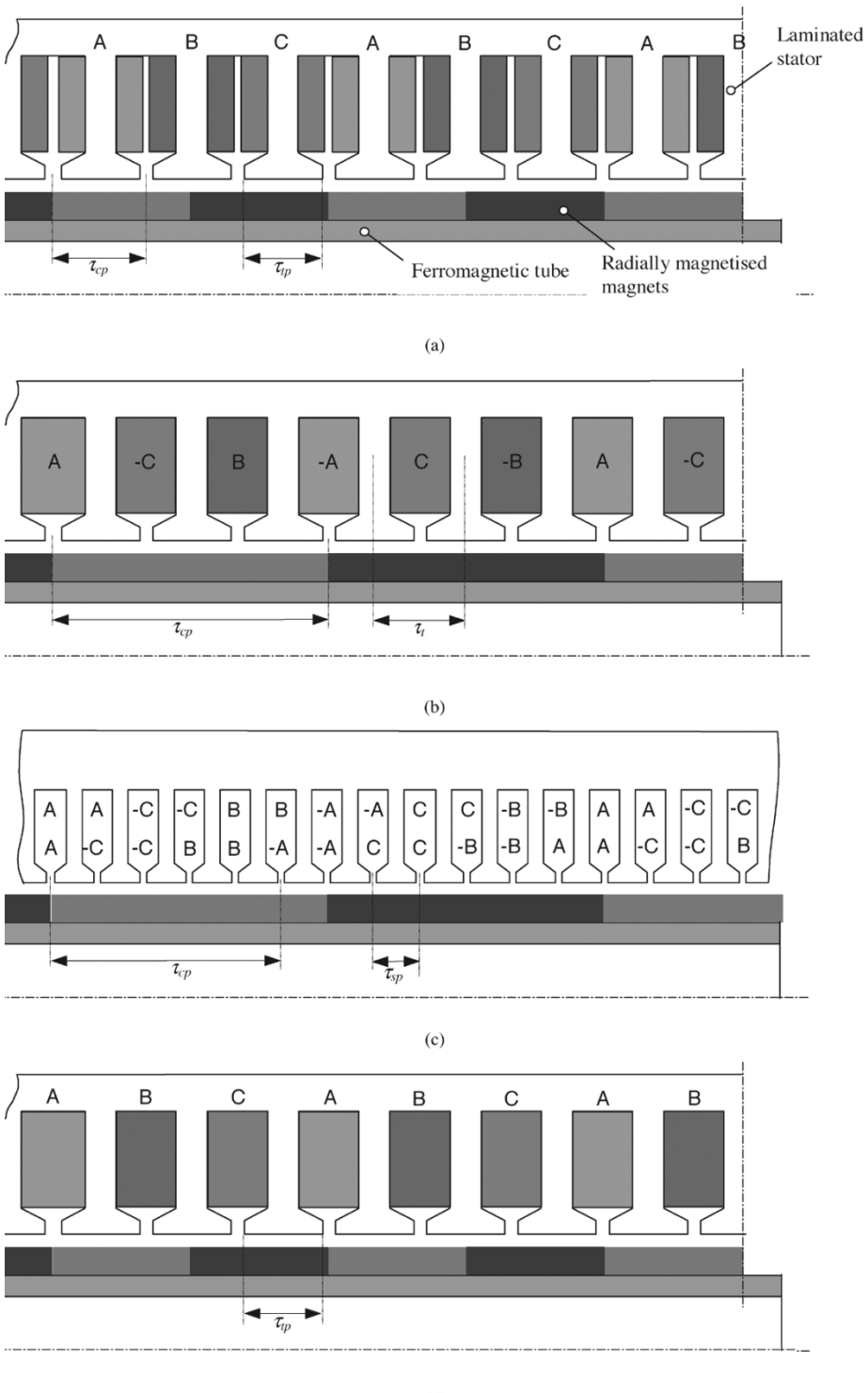

Fig. 1. Winding arrangements for three-phase tubular permanent-magnet machines. (a) Brushless dc winding (two coils per pole-pair per phase). (b) Brushless ac winding (full-pitched, one slot per pole per phase). (c) Brushless ac winding (short-pitched, two slots per pole per phase). (d) Brushless ac winding (one slot per pole-pair per phase).

Thus, the armature tooth-pitch is two thirds of a pole-pitch, and the ratio of the slot number to the pole number is 1.5. However, while the stator winding of a rotary brushless dc machine winding has a short coil-pitch, and, hence, a short end-winding, which is conducive to a high efficiency and a high power/force density, in a tubular brushless dc machine which has no end-windings this advantage no longer exists, and indeed the short coil-pitch leads to a lower winding factor for the fundamental electromotive force (EMF). Hence, a brushless dc winding is less favorable compared with conventional brushless ac windings.

B. Brushless AC

A conventional three-phase brushless ac winding has a 60° phase-spread and can be either full-pitched [Fig. 1(b)] or short-pitched [Fig. 1(c)]. A short-pitched winding is often used

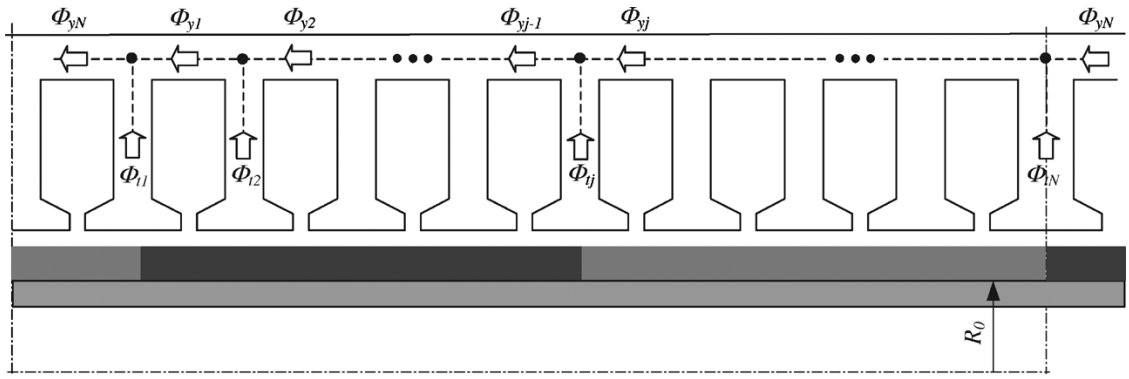

Fig. 2. Schematic of no-load flux distribution over N teeth.

to reduce EMF harmonics and force ripple while providing a greater degree of freedom in selecting an appropriate ratio of slot number to pole number, primarily to minimize the cogging force. However, in order to eliminate low-order EMF harmonics (e.g., fifth and seventh) without a significant reduction in the winding factor, a short-pitched winding requires a minimum of two slots per pole per phase [Fig. 1(c)], which results in a relatively large number of slots. This may be a disadvantage from the manufacturing point of view, since it is then more difficult to laminate a tubular stator. Thus, a full-pitched winding, with one slot per pole per phase [Fig. 1(b)], is often used. In both cases, however, a conventional brushless ac winding results in an integer ratio of slot number to pole number, which results in a relatively large cogging force. For tubular machines, a further winding variant exists with one slot per pole-pair per phase, as shown in Fig. 1(d). This has the same slot number to pole number ratio as the brushless dc winding, but requires only one coil per pole-pair per phase. It is, therefore, easier to manufacture. However, it can be shown that this winding arrangement gives rise to a dc component in its magnetomotive force (MMF) distribution and has a slightly larger winding inductance, which leads to a lower power factor.

III. Flux-Linkage, EMF, and Thrust Force

For permanent-magnet machines with a slotted stator, the effect of slotting may be accounted for by introducing a Carter coefficient K_c, given by [19], [20]

$$K_c = \frac{\tau_t}{\tau_t - \gamma g'} \tag{1}$$

where $g' = G + h_m/\mu_r$, τ_t is the stator slot-pitch, G is the air-gap length, μ_r is the relative recoil permeability of the permanent magnets and h_m is their radial thickness, and the slotting factor γ is given by

$$\gamma = \frac{4}{\pi}\left\{\frac{b_0}{2g'}\tan^{-1}\left(\frac{b_0}{2g'}\right) - \ln\sqrt{1+\left(\frac{b_0}{2g'}\right)^2}\right\} \tag{2}$$

where b_0 is the width of the stator slot openings. Therefore, the effective air gap g_e and the equivalent armature bore radius R_{se} are given, respectively, by

$$g_e = G + (K_c - 1)g' \tag{3}$$

$$R_{se} = R_m + g_e \tag{4}$$

where R_m is the outer radius of the magnets. It has been shown in [17] that the flux-linkage of a phase winding is given by

$$\Psi_{pw} = \sum_{n=1,2,\ldots}^{\infty} \Phi_{np} \cos m_n \left(z - \frac{\tau_{cp}}{2}\right) \tag{5}$$

where

$$m_n = \frac{(2n-1)\pi}{\tau_p} \tag{6}$$

and

$$\Phi_{np} = \frac{4\pi p N_c K_{dpn}}{m_n} K_{rn} \tag{7}$$

where p is the number of pole-pairs, τ_p is the pole-pitch, N_c is the number of series turns per pole, and τ_{cp} is the coil-pitch. For a brushless ac machine with one slot per pole-pair [Fig. 1(d)], $\tau_{cp} = 0$. K_{dpn} is defined as the winding factor of the $(2n-1)$th harmonic, and is dependent on the winding type. K_{rn} is a coefficient related to the $(2n-1)$th harmonic in the radial air gap field distribution, and is given by

$$K_{rn} = R_{se}\left[a_{In} BI_1(m_n R_{se}) + b_{In} BK_1(m_n R_{se})\right] \tag{8}$$

where $BI_1(\bullet)$ and $BK_1(\bullet)$ are modified *Bessel* functions of the first and second kind, respectively, of order one. a_{In} and b_{In} are the coefficients of the $(2n-1)$th harmonic associated with the radial magnetization in the air-gap region, and are dependent on the permanent-magnet material properties and geometric parameters [17].

The induced EMF in each phase winding is given by

$$e_{pw} = -\frac{d\Psi_{pw}}{dt} = -\nu \sum_{n=1,2,\ldots}^{\infty} K_{En} \sin m_n \left(z - \frac{\tau_{cp}}{2}\right) \tag{9}$$

where v is the linear velocity of the armature, and K_{En} is the EMF constant of the $(2n-1)$th harmonic, and is given by

$$K_{En} = 4\pi p N_c K_{dpn} K_{rn}. \tag{10}$$

The winding factor K_{dpn} comprises of the pitch factor K_{pn} and the distribution factor K_{dn}. The pitch factor can be calculated from

$$K_{pn} = \begin{cases} \sin\left(\frac{m_n \tau_{cp}}{2}\right), & \text{For a bipolar winding} \\ & \{\text{Fig. 1(a)–(c)}\} \\ 1, & \text{For a homopolar winding} \\ & \{\text{Fig. 1(d)}\}. \end{cases} \tag{11}$$

For a brushless dc machine [Fig. 1(a)], τ_{cp} is equal to $2\tau_p/3$. Thus, for the fundamental component of EMF, $K_{p1} = \sin(60^0) = 0.866$, which is $\sim$13% lower than that for a nonchorded, brushless ac winding [Fig. 1(b)]. The distribution factor K_{dn} is given by

$$K_{dn} = \begin{cases} \dfrac{\sin\left(\frac{m_n b_0}{2}\right)}{\left(\frac{m_n b_0}{2}\right)}, & \text{For a brushless dc machine} \\ \dfrac{\sin\left(\frac{N_s m_n \tau_{sp}}{2}\right)}{N_s \sin\left(\frac{m_n \tau_{sp}}{2}\right)} \dfrac{\sin\left(\frac{m_n b_0}{2}\right)}{\left(\frac{m_n b_0}{2}\right)}, & \text{For a brushless ac machine} \end{cases} \tag{12}$$

where N_s is the number of coils per pole per phase, and τ_{sp} is the axial displacement between two adjacent coils. For windings with one slot per pole per phase or one slot per pole-pair per phase, as shown Fig. 1(b) and (d), respectively, $\tau_{sp} = 0$, and K_{dn} is the same as that for the brushless dc winding.

The instantaneous power of each phase when excited with current i is given by

$$P_e = e_{pw} \cdot i = -vi \sum_{n=1,2,\ldots}^{\infty} K_{En} \sin m_n \left(z - \frac{\tau_{cp}}{2}\right) \tag{13}$$

and the instantaneous force is

$$F_{wp} = \frac{P_e}{v} = -i \sum_{n=1,2,\ldots}^{\infty} K_{En} \sin m_n \left(z - \frac{\tau_{cp}}{2}\right). \tag{14}$$

However, the current i is related to the total slot area per pole per phase S_{AP}, the coil packing factor P_f, the current density J, and the number of turns per coil N_c by

$$i = \frac{J S_{AP} P_f}{N_c} \tag{15}$$

thus

$$F_{wp} = J P_f \sum_{n=1,2,\ldots}^{\infty} K_n \sin m_n \left(z - \frac{\tau_{cp}}{2}\right) \tag{16}$$

where $K_n = 4\pi p K_{dpn} K_{rn} S_{AP}$. For a three-phase machine carrying balanced sinusoidally time-varying currents, the current density in the phase windings is given by

$$\begin{aligned} J_A &= \sqrt{2} J_{\text{rms}} \sin\left(\omega t - \frac{\tau_{cp}}{2}\right) \\ J_B &= \sqrt{2} J_{\text{rms}} \sin\left(\omega t - \frac{\tau_{cp}}{2} - \frac{2\pi}{3}\right) \\ J_C &= \sqrt{2} J_{\text{rms}} \sin\left(\omega t - \frac{\tau_{cp}}{2} + \frac{2\pi}{3}\right) \end{aligned} \tag{17}$$

where J_{rms} is the rms current density and ω is the electrical angular frequency, which is related to the armature velocity v by $\omega = \pi v/\tau_p$. The total thrust force is obtained from

$$\begin{aligned} F &= F_A + F_B + F_C \\ &= \sqrt{2} J_{\text{rms}} \sum_{n=1}^{\infty} K_n \left[\sin m_n \left(z - \frac{\tau_{cp}}{2}\right) \sin\left(\omega t - \frac{\tau_{cp}}{2}\right) \right. \\ &\quad + \sin m_n \left(z - \frac{\tau_{cp}}{2} - \frac{2\tau_p}{3}\right) \sin\left(\omega t - \frac{\tau_{cp}}{2} - \frac{2\pi}{3}\right) \\ &\quad \left. + \sin m_n \left(z - \frac{\tau_{cp}}{2} + \frac{2\tau_p}{3}\right) \cos\left(\omega t - \frac{\tau_{cp}}{2} + \frac{2\pi}{3}\right) \right]. \end{aligned} \tag{18}$$

This may be simplified to

$$\begin{aligned} F = F_1 &+ \sum_{\substack{n=3k+1 \\ k=1,2\ldots}}^{\infty} F_{n1} \cos\left[(2n-2)\left(\frac{\pi z}{\tau_p}\right)\right] \\ &+ \sum_{\substack{n=3k+3 \\ k=0,1,2\ldots}}^{\infty} F_{n3} \cos\left[(2n-5)\left(\frac{\pi z}{\tau_p}\right)\right] \end{aligned} \tag{19}$$

where F_1, F_{n1}, and F_{n3} are given by

$$\begin{aligned} F_1 &= -\sqrt{2} K_1 J_{\text{rms}} P_f \frac{3}{2} \\ F_{n1} &= \sqrt{2} J_{\text{rms}} \frac{3}{2} K_n (-1)^k, \\ &\qquad n = 3k+1,\ k = 1, 2, \ldots \\ F_{n3} &= \sqrt{2} J_{\text{rms}} \frac{3}{2} K_n (-1)^{k+1}, \\ &\qquad n = 3k+3,\ k = 0, 1, 2, \ldots \end{aligned} \tag{20}$$

As will be evident from (20), the force ripple due to triple harmonics in the radial field distribution is zero. The normalized total force ripple is, therefore, given by

$$\text{TFR} = \frac{\sqrt{\sum_{n=3} F_n^2}}{F_1} = \frac{\sqrt{\sum_{n=3} K_n^2}}{K_1}, \quad n \neq 3k+2,\ k = 0, 1, 2, \ldots \tag{21}$$

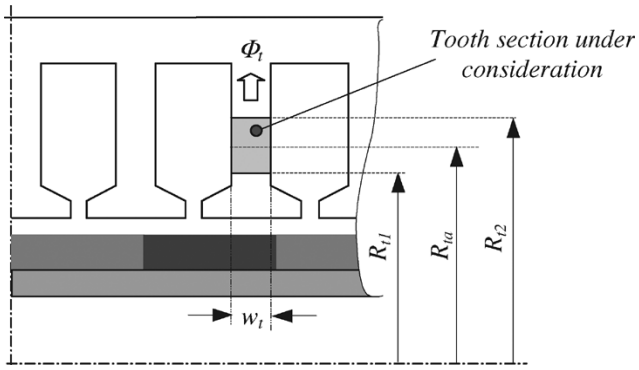

Fig. 3. Typical tooth section.

IV. No-Load Flux

A. No-Load Flux in Stator Teeth

The flux Φ_t that passes through a stator tooth can be calculated by integrating the radial flux density component at $r = R_{se}$ over the tooth tip width τ_{tp}. Thus

$$\Phi_t = \int_{z-\frac{\tau_{tp}}{2}}^{z+\frac{\tau_{tp}}{2}} 2\pi R_{se} B_r dz = \sum \frac{4\pi K_{rn}}{m_n} \sin\left(\frac{m_n \tau_{tp}}{2}\right) \sin m_n z. \tag{22}$$

This expression can be used to determine the required tooth width for a given maximum open-circuit flux density level.

B. No-Load Flux in Stator Yoke

Assuming that the magnetic field distribution repeats every N teeth, as illustrated in Fig. 2, then, if the reluctance of the jth yoke segment is denoted by R_{yj}, the fluxes in the teeth and the yoke segments are related by

$$\begin{aligned}
&R_{y1}\Phi_{y1} = R_{y1}\Phi_{y1}\\
&R_{y2}\Phi_{y2} = R_{y2}(\Phi_{y1} - \Phi_{t2})\\
&R_{y3}\Phi_{y3} = R_{y3}(\Phi_{y2} - \Phi_{t3}) = R_{y3}\Phi_{y1} - R_{y3}(\Phi_{t2} + \Phi_{t3})\\
&\vdots\\
&R_{yj}\Phi_{yj} = R_{yj}\Phi_{y1} - R_{yj}(\Phi_{t2} + \Phi_{t3} + \ldots + \Phi_{tj})\\
&\vdots\\
&R_{yN}\Phi_{yN} = R_{yj}\Phi_{y1} - R_{yj}(\Phi_{t2} + \Phi_{t3} + \ldots + \Phi_{tj}\\
&\qquad\qquad + \ldots + \Phi_{tN}).
\end{aligned} \tag{23}$$

Summing all the equations in (23) yields

$$\sum_{j=1}^{N} R_{yj}\Phi_{yj} = \Phi_{y1}\sum_{j=1}^{N} R_{yj} - \sum_{j=1}^{N-1}\left(\sum_{k=j+1}^{N} R_{yk}\right)\Phi_{t(j+1)}. \tag{24}$$

Due to the periodicity of the flux distribution over the N teeth, $\sum_{j=1}^{N} R_{yj}\Phi_{yj} = 0$. Thus

$$\Phi_{y1} = \frac{\left[\sum_{j=1}^{N-1}\left(\sum_{k=j+1}^{N} R_{yk}\right)\Phi_{t(j+1)}\right]}{\sum_{j=1}^{N} R_{yj}}. \tag{25}$$

Several observations may be made from (25), viz.

1) The fluxes in the yoke segments are related to all the fluxes in the N teeth and the reluctance of each yoke segment. When segments of the yoke are driven into saturation, (25) has to be used in an iterative manner in order to determine the yoke fluxes.
2) If the yoke is not saturated, the reluctance of each yoke segment is identical, and (25) reduces to

$$\Phi_{y1} = \frac{1}{N}\sum_{j=1}^{N-1}(N-j)\Phi_{t(j+1)}. \tag{26}$$

Thus, the yoke fluxes can be calculated from the N tooth fluxes.
3) For a brushless ac machine with an integer number of slots per pole, (26) can be further simplified to

$$\Phi_{y1} = \frac{1}{2}\sum_{j=1}^{N_P}\Phi_{tj} \tag{27}$$

where N_p is the number of slots per pole.
4) For a brushless dc machine, the flux distribution repeats every pole-pair (or three tooth-pitches), and (26) becomes

$$\Phi_{y1} = \frac{1}{3}(\Phi_{t3} + 2\Phi_{t2}). \tag{28}$$

Application of (26), (27), or (28) allows the fluxes in the yoke to be evaluated, and consequently enables it to be dimensioned for a specified maximum flux density.

C. No-Load Flux in Armature Yoke

The flux Φ_{ym} which passes through the ferromagnetic yoke at a given axial position z can be calculated by integrating the expression for $A_\theta(r,z)$, the vector magnetic potential, which is given in [17], around the circumference at $r = R_o$. Thus

$$\begin{aligned}
\Phi_{ym} &= \int_0^{2\pi} R_0 A_\theta(R_0, z)d\theta\\
&= 2\pi R_0 \sum \frac{a_{nII} BI_1(m_n R_0) + b_{nII} BK_1(m_n R_0)}{m_n} \sin m_n z
\end{aligned} \tag{29}$$

where a_{IIn} and b_{IIn} are the coefficients of the $(2n-1)$th harmonic associated with the radial magnetization in the magnet

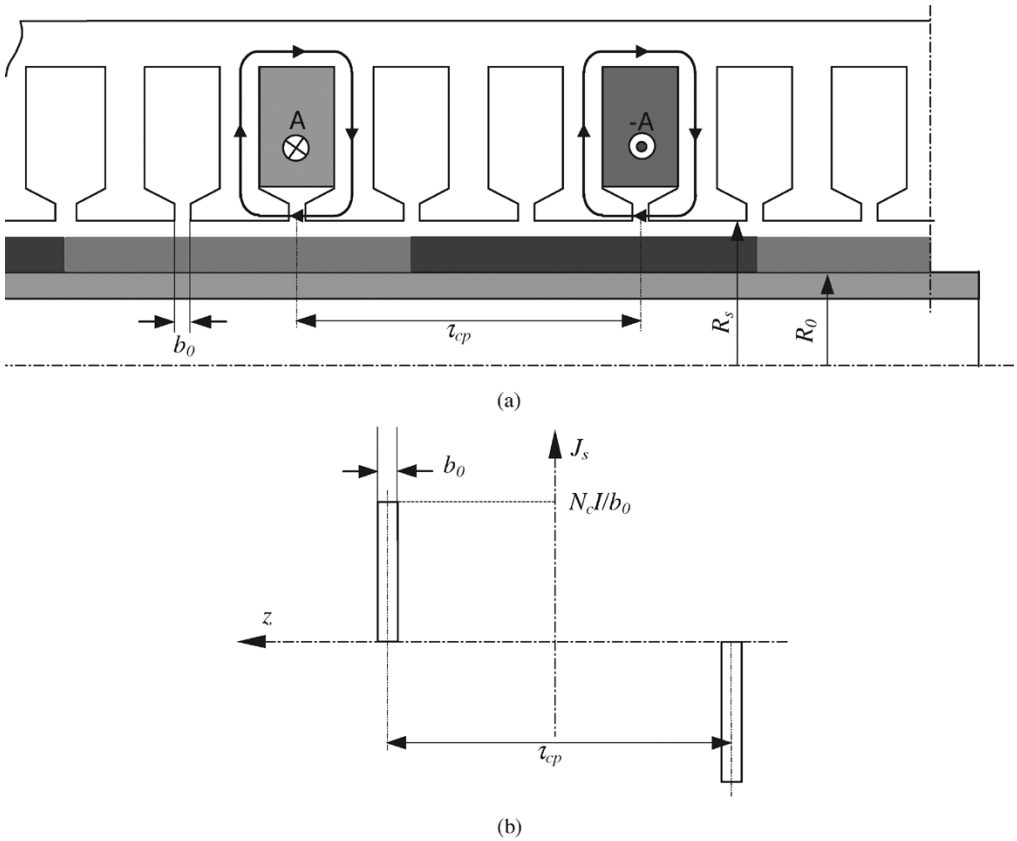

Fig. 4. Current distribution due to one phase winding of a brushless machine with one slot per pole per phase. (a) Actual current distribution. (b) Equivalent current sheet distribution.

region, and are given in [17]. This expression can be used to determine the required radial thickness of the tubular yoke for a specified maximum flux density level.

V. Open-Circuit Iron Loss

Once the dimensions of the stator teeth and yoke have been specified, the no-load flux density in the teeth and yoke can be obtained, by dividing (22) and (25) by the corresponding cross-sectional areas. For parallel-sided teeth, the tooth area increases linearly with the radius. Thus, a tooth can be divided into a number of sections along its radial length, and within each section the flux density can be assumed to be constant. The open-circuit iron loss density (i.e., with no account of the armature reaction field) in the yoke and each section of the teeth can then be estimated using (30), which has been validated extensively [21]

$$P_{fe} = K_h \cdot f \cdot B_m^{\alpha} + \frac{K_e}{T}\int_T \left|\frac{dB(t)}{dt}\right|^{1.5} dt + \frac{\sigma l_{fe}^2}{12\delta}\frac{1}{T}\int_T \left(\frac{dB(t)}{dt}\right)^2 dt \tag{30}$$

where P_{fe} is the iron loss density, and K_h and α are constants related to the hysteresis iron loss component. K_e is the excess eddy-current loss constant, f and T are the fundamental frequency and period, B_m is the peak flux density, σ and δ are the electrical conductivity and mass density of the lamination material, l_{fe} is the thickness of the lamination. K_h, α, and K_e are determined experimentally for the particular grade of stator lamination material.

However, when calculating the total open-circuit iron loss of a region, the tubular geometry of the stator must be taken into account. For example, if the average radius of a stator tooth section is R_{ta}, then, from (22), the average flux density and its time derivative are given by

$$\begin{aligned} B_{ta} &= \frac{1}{2\pi R_{ta}} \sum \frac{4\pi K_{rn}}{m_n} \sin\left(\frac{m_n \tau_{tp}}{2}\right) \sin m_n z \\ &= \frac{1}{R_{ta}} \sum \frac{2K_{rn}}{m_n} \sin\left(\frac{m_n \tau_{tp}}{2}\right) \sin m_n z \end{aligned} \tag{31}$$

$$\begin{aligned} \frac{dB_{ta}}{dt} &= \frac{1}{R_{ta}} \sum 2K_{rn} \sin\left(\frac{m_n \tau_{tp}}{2}\right) \cos m_n z \frac{dz}{dt} \\ &= \frac{v}{R_{ta}} \sum 2K_{rn} \sin\left(\frac{m_n \tau_{tp}}{2}\right) \cos m_n z. \end{aligned} \tag{32}$$

Thus, the loss density P_{fet} in the tooth section can be calculated analytically and the total iron loss P_{it} obtained by integrating over the region

$$P_{it} = P_{fet} \pi \left(R_{t2}^2 - R_{t1}^2\right) w_t \delta \tag{33}$$

where w_t is the tooth width, and R_{t1} and R_{t2} are the inner and outer radii of the tooth section, as shown in Fig. 3. The total open-circuit iron loss is then obtained by summing the losses in all the regions of the stator.

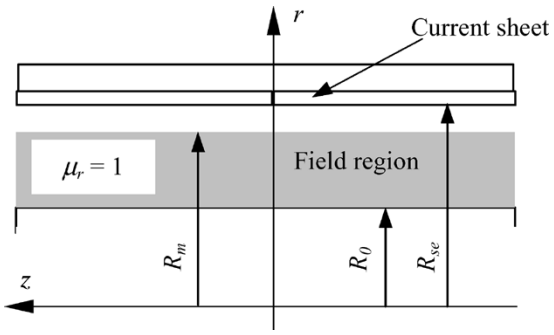

Fig. 5. Armature reaction field model.

VI. Armature Reaction Field

A. Current Distribution in Conventional Brushless Permanent-Magnet Machines

The current distribution in the conventional slotted stators [Fig. (1a)–(c)] may be represented using a current sheet model [22], as illustrated in Fig. 4. Assuming the yoke and teeth to be infinitely permeable, then, according to Ampere's law, the ampere-conductors N_cI in a slot may be represented by an equivalent current sheet N_cI/b_0 distributed over the width of the slot opening b_0. The current distribution in Fig. 4(b) may be expanded into a Fourier series over a period of $2\tau_p$, viz.

$$J_s(z) = \frac{2N_cI}{\tau_p} \sum_{n=1,2,\ldots}^{\infty} K_{dcn} K_{pcn} \sin m_{cn} z \tag{34}$$

where

$$\begin{aligned} m_{cn} &= \frac{n\pi}{\tau_p} \\ K_{dcn} &= \frac{\sin\left(\frac{m_{cn}b_0}{2}\right)}{\left(\frac{m_{cn}b_0}{2}\right)} \\ K_{pcn} &= \sin\left(\frac{m_{cn}\tau_{cp}}{2}\right). \end{aligned} \tag{35}$$

B. Armature Reaction Field

The effect of stator slotting can be taken into account by assuming the equivalent stator bore radius R_{se} in (4). If, for simplicity, the relative recoil permeability of the magnets is assumed to be 1, i.e., $\mu_r = 1$, the armature reaction field may be deduced from the model shown in Fig. 5. The governing field equation, in terms of the vector magnetic potential A_θ, is given by

$$\frac{\partial}{\partial z}\left(\frac{1}{r}\frac{\partial}{\partial z}(rA_\theta)\right) + \frac{\partial}{\partial r}\left(\frac{1}{r}\frac{\partial}{\partial r}(rA_\theta)\right) = 0. \tag{36}$$

The boundary conditions to be satisfied by (36) are

$$B_z|_{r=R_{se}} = \mu_0 J_s(z); \quad B_z|_{r=R_0} = 0. \tag{37}$$

Solving (36) subject to the boundary conditions of (37) yields the following expressions for A_θ and the flux density components:

$$\begin{aligned} A_\theta = \sum_{n=1,2,\ldots} \frac{I}{m_{cn}} &\{a_{an} BI_1(m_{cn}r) + b_{an} BK_1(m_{cn}r)\} \\ &\times \sin m_{cn} z \end{aligned} \tag{38}$$

$$\begin{aligned} B_r(r,z) = &- I \sum_{n=1,2,\ldots}^{\infty} [a_{an} BI_1(m_{cn}r) + b_{an} BK_1(m_{cn}r)] \\ &\times \cos(m_{cn} z) \\ B_z(r,z) = &I \sum_{n=1,2,\ldots}^{\infty} [a_{an} BI_0(m_{cn}r) - b_{an} BK_0(m_{cn}r)] \\ &\times \sin(m_{cn} z) \end{aligned} \tag{39}$$

where the harmonic field coefficients a_{an} and b_{bn} are given in the Appendix. Equation (39) provides a basis for evaluating the extent of any partial irreversible demagnetization of the magnets which may occur under any specified operating condition.

C. Self and Mutual Inductances

The flux-linkage of a phase winding having p pole-pairs due to its own armature reaction field may be obtained by integration of A_θ, and is given by

$$\psi_{wap} = \frac{2N_c}{b_0} \int_{\frac{\tau_{pc}}{2}-\frac{b_0}{2}}^{\frac{\tau_{pc}}{2}+\frac{b_0}{2}} 2\pi R_{se} A_\theta(R_{se}, z)\, dz \tag{40}$$

which yields

$$\begin{aligned} \psi_{wap} = I \sum_{n=1,2,\ldots} \frac{4\pi N_c R_{se}}{m_{cn}} &[a_{an} BI_1(m_{cn}R_{se}) \\ &+ b_{an} BK_1(m_{cn}R_{se})]\, K_{dcn} K_{pcn}. \end{aligned} \tag{41}$$

The air-gap component of the winding self-inductance is, therefore, given by

$$\begin{aligned} L_{sa} = \frac{\psi_{wap}}{I} = \frac{8\pi\mu_0 p R_{se} N_c^2}{\tau_p} &\sum_{n=1,2,\ldots}^{\infty} \frac{(K_{dcn}K_{pcn})^2}{m_{cn}\Delta_n} \\ &\times [c_{2n} BI_1(m_{cn}R_{se}) + c_{1n} BK_1(m_{cn}R_{se})] \end{aligned} \tag{42}$$

where c_{1n}, c_{2n} and Δ_n are given in the Appendix. The mutual inductance M_{ij} between phases i and j ($i \neq j$) separated by an axial distance τ_{ij} can be similarly deduced, and is given by

$$\begin{aligned} M_{ija} = \frac{8\pi\mu_0 p R_{se} N_c^2}{\tau_p} &\sum_{n=1,2,\ldots}^{\infty} \frac{(K_{dcn}K_{pcn})^2}{m_{cn}\Delta_n} \\ &\times [c_{2n} BI_1(m_{cn}R_{se}) + c_{1n} BK_1(m_{cn}R_{se})] \cos m_{cn}\tau_{ij} \end{aligned} \tag{43}$$

It should be noted that the MMF distribution of a homopolar winding with one slot per pole-pair per phase, as shown in Fig. 1(d), contains a dc component, and its field solution needs to be analyzed separately. However, this is beyond the scope of the paper. The foregoing equations for the armature reaction field and inductances are applicable to the winding configurations shown in Fig. (1a)–(c).

For a slotted stator, however, slot leakage will also contribute to the self and mutual inductances, and may be analyzed by the model shown in Fig. 6. Assuming that the stator core is infinitely permeable and that the cross-slot leakage flux is parallel to the z axis, the flux density at a distance x from the bottom of the slots is given by

$$B_{sk} = \mu_0 \frac{N_c I}{S_w h_s} x. \tag{44}$$

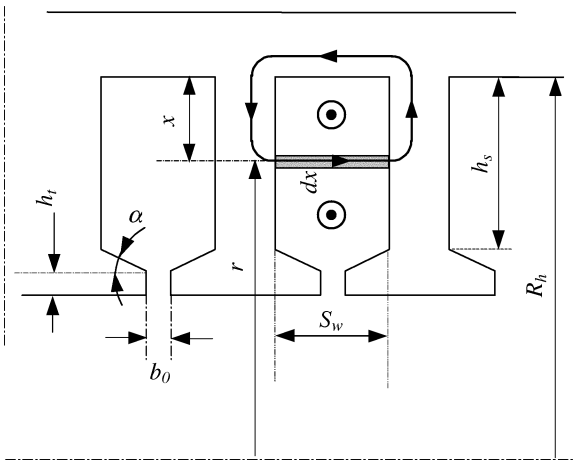

Fig. 6. Slot leakage model.

The flux which passes through an area of length of $2\pi r$ and depth dx is, therefore, given by

$$d\Phi_{sk} = 2\pi r dx B_{sk} = 2\pi(R_h - x)\mu_0 \frac{N_c I}{S_w h_s} x dx. \tag{45}$$

This flux links with $N_c x/h_s$ turns, and, hence, the partial flux-linkage is given by

$$d\Psi_{sk} = \frac{N_c x}{h_s} d\Phi_{sk} = 2\pi\mu_0 \frac{N_c^2 I}{S_w h_s^2}(R_h - x)x^2 dx. \tag{46}$$

The total flux-linkage over the current carrying region of the slot is, therefore

$$\Psi_{sk} = \int_0^h d\Psi_{sk} = \frac{2\pi\mu_0 N_c^2 I h_s}{S_w}\left(\frac{R_h}{3} - \frac{h_s}{4}\right). \tag{47}$$

The total slot leakage inductance, including components associated with the tooth tip height h_t and the taper angle α, is given by

$$L_{sk} = 4\pi\mu_0 p N_{sp} N_c^2 \left[\frac{h_s}{S_w}\left(\frac{R_h}{3} - \frac{h_s}{4}\right) + (R_s + h_t)\left(\frac{h_t}{b_0} + \frac{S_w - b_0}{S_w + b_0}\tan\alpha\right)\right] \tag{48}$$

where N_{sp} is the number of slots per pole per phase. A similar expression can be derived for the slot leakage component of the mutual inductance M_{sk}. Thus, the total self and mutual inductances are given by

$$\begin{aligned} L_{sp} &= L_{sa} + L_{sk} \\ M_{ij} &= M_{ija} + M_{sk}. \end{aligned} \tag{49}$$

D. Effect of Saturation

The analytical field solutions for the no-load and armature reaction magnetic field distributions have been derived assuming that the armature and stator cores are highly permeable. In many practical designs, however, this may not be the case. In order to account for the effect of core saturation, a fictitious radial air gap is introduced between the inner bore of the stator and the outer surface of the magnets. As has been described in Section IV, the no-load fluxes in the stator teeth and yoke, and in the armature yoke, can be evaluated analytically, while the peak flux density in these regions, taking account of the armature reaction field, can be obtained from

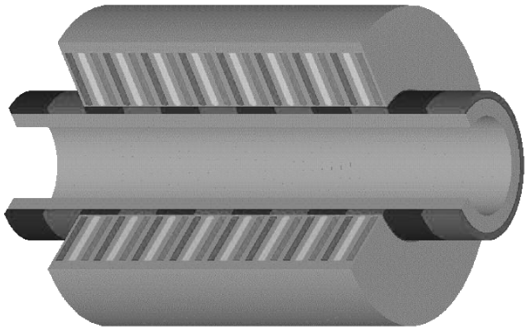

Fig. 7. Schematic of radially magnetized tubular permanent magnet machine.

$$B_{mrj} = \frac{B_{m0}}{\cos\varphi_s} \tag{50}$$

where B_{m0} and B_{mrj} are the no-load and resultant peak flux densities in the jth region, respectively, $\cos\varphi_s$ is the power factor at a specified load condition, and j denotes one of the three regions: viz., the stator teeth, the stator yoke, or the armature yoke, where saturation is of concern. The total MMF drop due to saturation can be written as

$$F = \sum_j H_{mrj} l_j \tag{51}$$

where H_{mrj} is the resultant magnetic field strength in the jth region, which can be deduced from the calculated flux density and the B–H characteristic of the core material, and l_j is the average length of the flux path in the jth region. The length of the fictitious air gap ΔG may then be determined from

$$\Delta G = \frac{F}{B_{am}/\mu_0} \tag{52}$$

where B_{am} is the peak no-load flux density at the stator bore, viz., at $r = R_{se}$. The winding flux-linkage due to the permanent magnets, the thrust force, the armature reaction field, and the winding inductances, can therefore all be calculated analytically using the equivalent air-gap $g_e + \Delta G$. The effectiveness of this procedure has been confirmed by finite-element analysis, as will be shown in the next section, and it could be employed to account for the effect of saturation under any load condition from a knowledge of the power factor for that condition.

VII. Validation by Finite-Element Analysis

The main design parameters of the radially magnetized, three-phase, one slot per pole per phase tubular machine shown in Fig. 7, for which analytical field solutions have been obtained, are given in Table I. The stator extends over four active pole-pairs, and the magnets are sintered NdFeB with a remanence $B_{\rm rem} = 1.15$ T and $\mu_r = 1.05$. The derived analytical expressions for the field distribution have been validated by finite-element calculations of the radial and axial flux density components in various regions of the machine.

TABLE I
LEADING DESIGN PARAMETERS OF TUBULAR MACHINE (M)

R_e	R_m	h_m	G	τ_p
0.1	0.0468	0.005	0.001	0.0276
τ_m/τ_p	b_0	h_t	h_s	τ_{cp}
1.0	0.002	0.001	0.014	0.0276

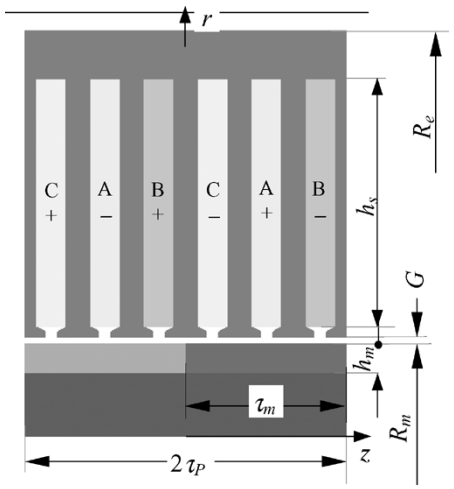

Fig. 8. Finite-element model.

The finite-element solutions were obtained using the model shown in Fig. 8 by applying a periodic boundary condition at the axial boundaries $z = \pm\tau_p$ and imposing the natural Dirichlet boundary condition at the other bounding surfaces. Saturation of the stator and armature cores was accounted for by using the B–H curves for the respective ferromagnetic materials. The finite-element model thus takes into account all key effects, such as nonlinearity and slotting, which a practical machine may exhibit.

Fig. 9 compares analytically predicted and finite-element-calculated open-circuit distributions of the axial and radial flux density components B_{Iz} and B_{Ir} as functions of the axial position z at the center of the air gap, viz., at radius $r = 0.0473\,(\mathrm{m})$, and with zero axial displacement between the stator and armature, while Fig. 10 shows the flux distributions for two displacements, viz., $z_d = 0$ and $z_d = \tau_p/2$. It will be seen that the analytical prediction agrees well with the finite-element solution, the main discrepancies being in regions close to the slot openings, which are, of course, not taken into account in the analytical model.

Fig. 11 compares the analytically predicted and finite-element-calculated EMF waveform per turn for a constant armature velocity of 1 (m/s). As will be seen, excellent agreement is again achieved. A comparison of the analytically predicted and finite-element-calculated thrust force which results with the rated three-phase sinusoidal current excitation is given in Fig. 12. Again, good agreement is achieved in both the amplitude and the waveform. It will be noted that both models predict a significant force ripple, due mainly to the presence of the fifth harmonic in the EMF waveforms.

It should also be noted that the finite-element predicted force waveform contains the tooth ripple cogging force component, which is also shown separately in Fig. 12, and that the average force is slightly lower than that predicted from the analytical model, due mainly to the effect of localized saturation, which may not be fully accounted for using the technique described in Section VI-D.

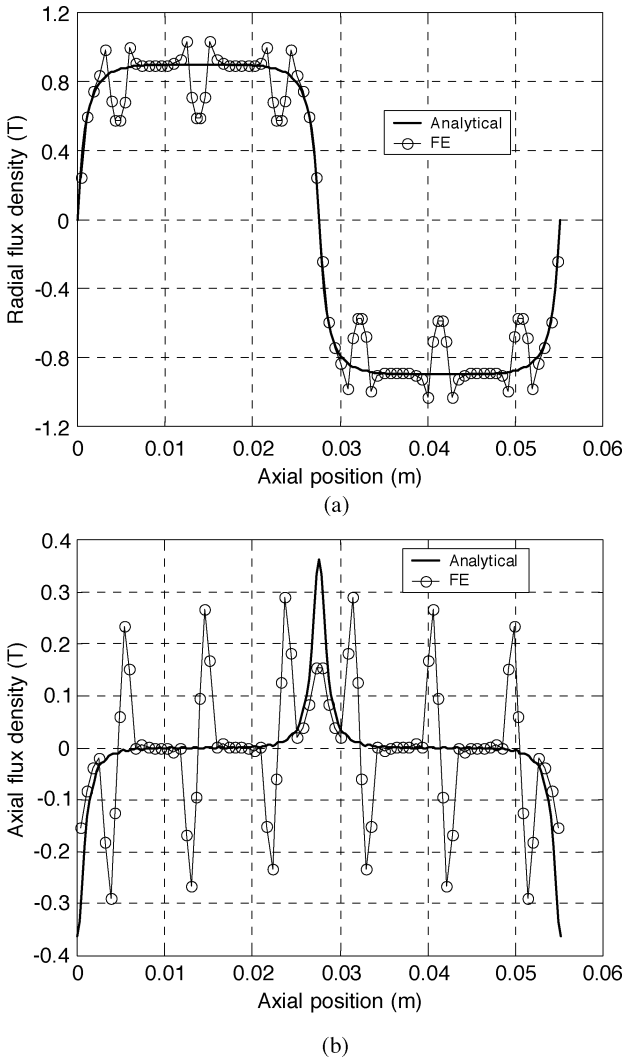

Fig. 9. Comparison of flux density in air gap as a function of z at $r = 0.0473$, for $z_d = 0$. (a) Radial component. (b) Axial component.

Fig. 13 shows a comparison of the analytically predicted and finite-element-calculated distribution of the radial component of the armature reaction field in the center of the air gap when phase A is excited with rated current. In Fig. 13(a), the effect of core saturation, which is significant at full load, is neglected in the analytical model, and consequently it predicts a flux density which is ∼20% higher than the finite-element calculation. When core saturation is accounted for, by using the procedure described in Section VI-D, the difference between the analytical prediction and finite-element calculation is significantly reduced [Fig. 13(b)].

Table II compares analytically and finite-element-predicted self and mutual inductances, where good agreement is again achieved, the difference being less than 5%.

VIII. DESIGN OPTIMIZATION

A. Thermal Constraints

As can be seen from (20), the thrust force capability is proportional to the rms current density, which, in turn, is limited by

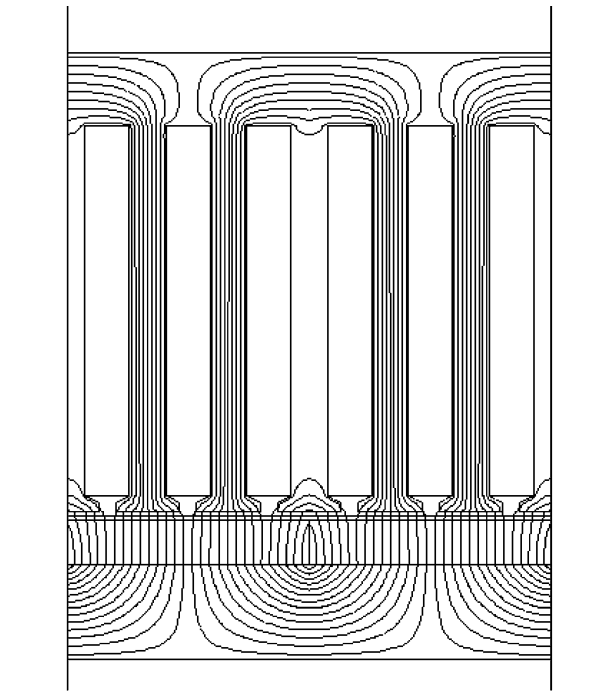

(a)

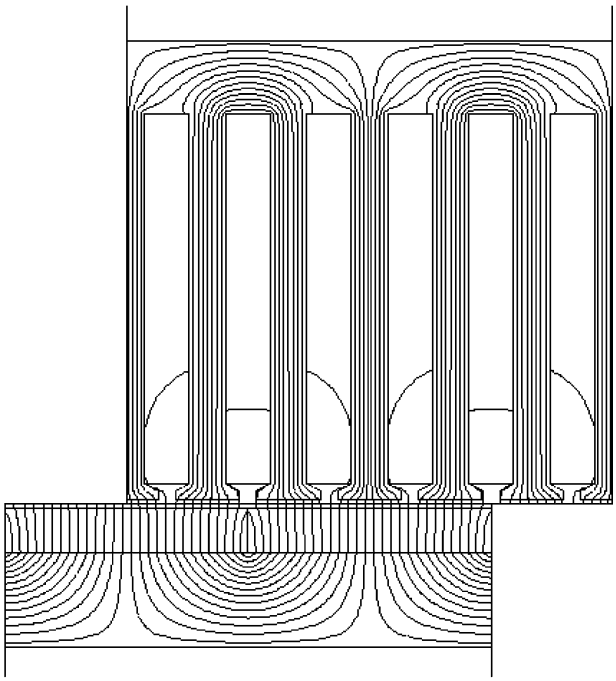

(b)

Fig. 10. Open-circuit flux distributions for two axial displacements. (a) $z_d = 0$. (b) $z_d = \tau_p/2$.

the allowable temperature rise, for a specific cooling arrangement. Hence, the permissible winding copper loss and iron loss are governed by the dissipation capability of the machine, i.e.,

$$V_s N_s P_f \rho J_{\rm rms}^2 + p_{fe} = k_\theta A \Delta T \tag{53}$$

where V_s is the current-carrying volume of a slot, N_s is the total number of slots, ρ is the resistivity of copper at a specified operating temperature, k_θ is the stator surface thermal dissipation

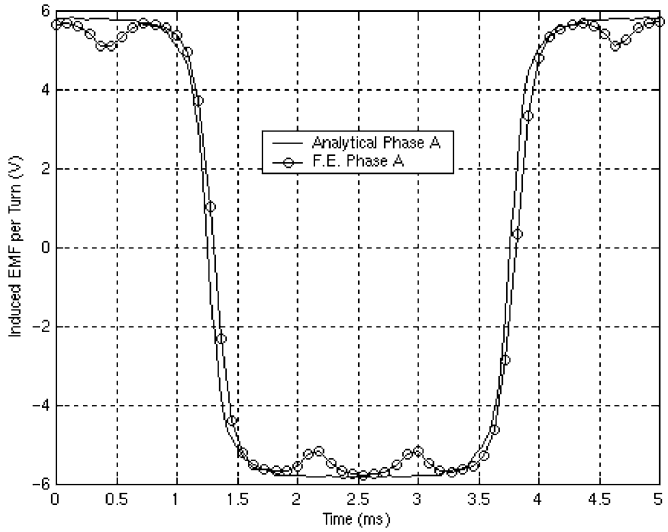

Fig. 11. Comparison of EMF per turn at $v = 1.0$ (m/s).

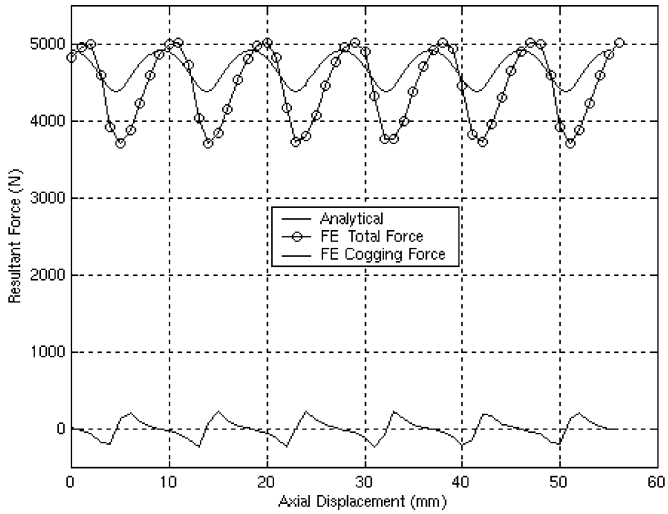

Fig. 12. Comparison of thrust force and tooth ripple cogging force as a function of armature position at rated current.

coefficient, A is the stator surface dissipation area, and ΔT is the allowable temperature rise of the windings. The iron loss p_{fe} can be predicted using the formula given in Section V from the flux density derived from the analytical field solution. With reference to Fig. 6, the volume of a slot can be calculated from

$$V_s = \pi \left(R_h^2 - R_i^2\right) S_w; \quad R_i = R_s - h_t - \frac{S_w - b_0}{2} \tan\alpha. \tag{54}$$

The permissible current density is, therefore, given by

$$J_{\rm rms} = \sqrt{\frac{k_\theta A \Delta T - p_{fe}}{\pi S_w \left(R_h^2 - R_i^2\right) P_f \rho N_s}}. \tag{55}$$

Thus, (20) and (55) relate the force capability to the design parameters under a given thermal condition.

B. Winding Design

In permanent-magnet brushless machines, the rms current density and, hence, the force capability is limited by the thermal constraint. For a given dc link voltage, the stator phase current

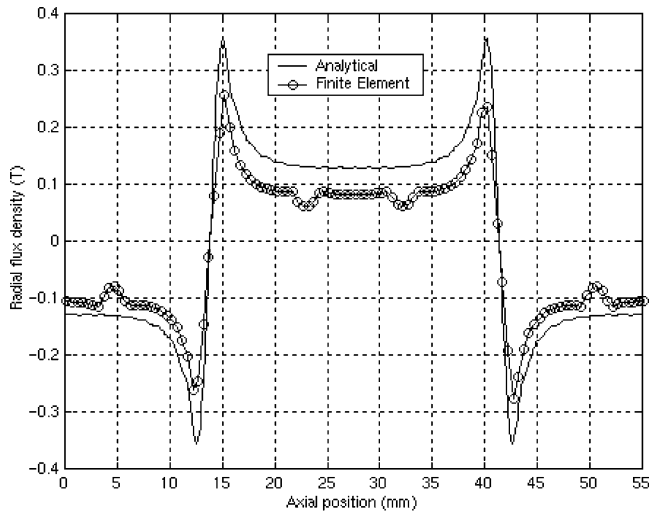

(a)

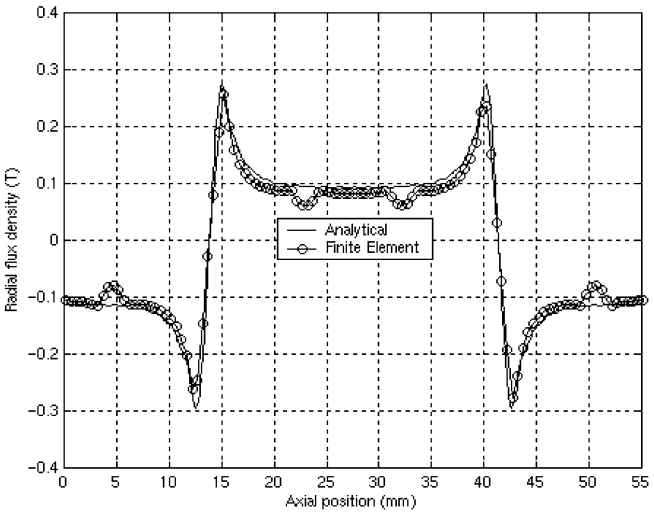

(b)

Fig. 13. Comparison of radial flux density component of armature reaction field. (a) Core saturation neglected. (b) Core saturation taken into account.

TABLE II
COMPARISON OF ANALYTICALLY PREDICTED AND FINITE-ELEMENT-CALCULATED INDUCTANCES (mH)

	Analytical	Finite Element
Self-inductance	0.473	0.425
Mutual inductance	0.030	0.045
Synchronous inductance	0.503	0.480

will be dependent on the maximum phase voltage, the phase back-EMF, and the synchronous impedance. Hence, in order to optimize the force capability of a given machine, specifically in terms of establishing the preferred pole number and "split-ratio" (i.e., the ratio of R_m to the outer stator radius R_e), it is necessary to calculate the synchronous impedance of the stator winding. The coil resistance can be calculated using

$$R = \left(\frac{2\pi R_{avc}\rho N_{spp}}{P_f S_a}\right) N_c^2 \tag{56}$$

where N_{spp} is the number of slots per phase, $R_{avc} = (R_h + R_i)/2$ is the average radius of a coil, and $S_a = S_w(R_h - R_i)$ is the slot area. The peak phase current I_m is related to the rms current density $J_{\rm rms}$ by

$$I_m = \frac{\sqrt{2}J_{\rm rms}S_a P_f}{N_c}. \tag{57}$$

Thus, the resistive voltage drop is given by

$$\begin{aligned} RI_m &= 2\sqrt{2}\pi J_{\rm rms}\rho N_{spp}N_c = K_{R0}N_c \\ K_{R0} &= 2\sqrt{2}\pi J_{\rm rms}\rho N_{spp} \end{aligned} \tag{58}$$

As has been shown in Section VI-C, the self and mutual inductances are proportional to the square of the number of turns per coil, N_c. Hence, the synchronous inductance can be related to N_c by

$$L_{sn} = \Lambda_{sn}N_c^2 \tag{59}$$

where the synchronous inductance coefficient Λ_{sn} is constant for a given machine design

$$\Lambda_{sn} = \frac{(L_{sp} + M_{ij})}{N_c^2}. \tag{60}$$

Thus, the reactance voltage at an armature velocity v is obtained from

$$\omega L_{sn}I_m = \frac{\pi v}{\tau_p}\frac{\Lambda_{sn}N_c^2\sqrt{2}J_{rms}S_aP_f}{N_c} = K_{L0}vN_c \tag{61}$$

where

$$K_{L0} = \frac{\pi}{\tau_p}\Lambda_{sn}\sqrt{2}J_{\rm rms}S_aP_f.$$

From (9) and (10), the peak fundamental back-EMF is related to the number of turns per coil by

$$E_m = K_{E0}vN_c. \tag{62}$$

Thus, if the stator current is controlled to be in phase with the induced EMF for maximum force per ampere operation, according to the phasor diagram in the d-q reference frame, the peak phase current is related to the peak applied voltage V_m by

$$(RI_m + E_m)^2 + (\omega L_{sn}I_m)^2 = V_m^2. \tag{63}$$

Substituting (58), (61), and (62) into (63) and solving for N_c yields

$$N_c = \frac{V_m}{\sqrt{(KR_0 + K_{E0}v)^2 + (K_{L0}v)^2}}. \tag{64}$$

The power factor can be evaluated from

$$\cos\varphi = \frac{(E_m \pm RI_m)}{V_m} \tag{65}$$

where the plus and minus signs correspond to motoring and generating modes of operation, respectively. If the machine is sup-

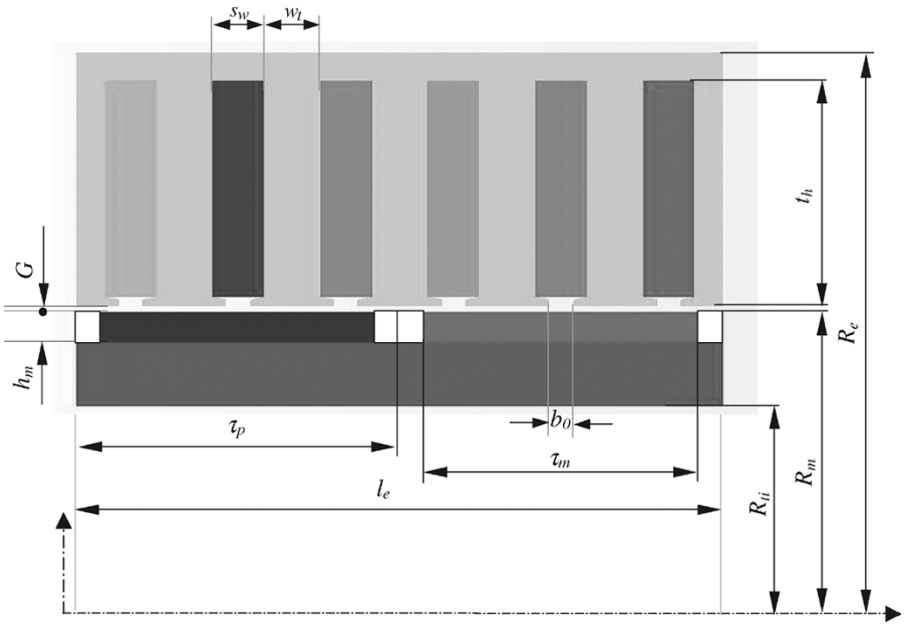

Fig. 14. Design parameters of radially magnetised, slotted tubular permanent-magnet machine.

plied from a converter with a dc link voltage of $V_{\rm dc}$, the maximum peak phase voltage V_m is dependent on the PWM scheme, viz.

$$V_m = \begin{cases} \dfrac{V_{\rm dc}}{2}, & \text{for sinusoidal pulsewidth modulation} \\ \dfrac{V_{\rm dc}}{\sqrt{3}}, & \text{for space vector pulsewidth modulation.} \end{cases} \tag{66}$$

C. Converter Losses

Since the VA rating and conduction loss of a converter are related to its rms current, a lower power factor machine implies both a higher VA rating and a higher rms current for the same output power. Hence, the converter VA rating and converter loss increase as the machine power factor decreases. Further, currently the cost of the power electronic converter usually dominates the overall cost of a drive system. Thus, the power factor as an output parameter of a machine design has a significant influence on both the drive system efficiency and cost. Therefore, a design optimization process for the machine should take the overall system performance and cost into account, rather than just considering the machine performance and cost independently.

The total converter loss P_{lc} of a voltage source converter comprises of the conduction loss, P_{cond}, of both the switches and diodes, the switching loss P_{sw}, and the reverse recovery loss P_{rrevc}, which can be calculated using the following equations [23], [24]:

$$P_{lc} = P_{cond} + P_{sw} + P_{rrevc} \tag{67}$$

$$\begin{aligned} P_{cond} = {} & \frac{6V_{ton}I_m}{2\pi}\left[1+\frac{\pi}{4}m_d\cos(\varphi)\right] \\ & + \frac{6R_{ton}I_m^2}{2\pi}\left[\frac{\pi}{4}+\frac{2}{3}m_d\cos(\varphi)\right] \\ & + \frac{6V_{don}I_m}{2\pi}\left[1-\frac{\pi}{4}m_d\cos(\varphi)\right] \\ & + \frac{6R_{don}I_m^2}{2\pi}\left[\frac{\pi}{4}-\frac{2}{3}m_d\cos(\varphi)\right] \end{aligned} \tag{68}$$

$$\begin{aligned} P_{rrevc} = {} & 6f_sV_{\rm dc}\left\{\left[0.28+\frac{0.38I_m}{\pi I_{cn}}+0.015\left(\frac{I_m}{I_{cn}}\right)^2\right]Q_{rnn}\right. \\ & \left. + \left(\frac{0.8}{\pi}+0.05\frac{I_m}{I_{cn}}\right)I_m t_{rnn}\right\} \end{aligned} \tag{69}$$

$$\begin{aligned} P_{sw} = {} & \frac{6V_{\rm dc}t_{rn}f_sI_m^2}{8I_{cn}} \\ & + 6V_{\rm dc}t_{fn}f_sI_m\left(\frac{1}{3\pi}+\frac{1}{24}\frac{I_m}{I_{cn}}\right) \end{aligned} \tag{70}$$

where

V_{on}	on-state voltage drop of power switch;
R_{ton}	on-state resistance of power switch;
V_{don}	on-state voltage drop of diode;
R_{don}	on-state resistance of diode;
I_m	peak line current of machine;
f_s	switching frequency;
m_d	modulation ratio of converter;
I_{cn}	rated device current;
Q_{rrn}	rated recovery charge;
t_{rrn}	rated reverse recovery time;
t_{rr}	rated rise time;
t_{fn}	rated fall time.

The device parameters for use in the foregoing equations can be obtained from the manufacturer's data sheets for the power semiconductors that are used in the converter.

D. Influence of Leading Design Parameters on Machine and Drive System Performance

The main design parameters that influence the electromagnetic performance of a slotted tubular machine are shown in Fig. 14, where l_e is the active armature length, G is the air-gap length, and R_e is the outer radius of the stator. It should be noted that the tooth width w_t and the stator and armature yoke dimensions are dependent on the air-gap flux density and the max-

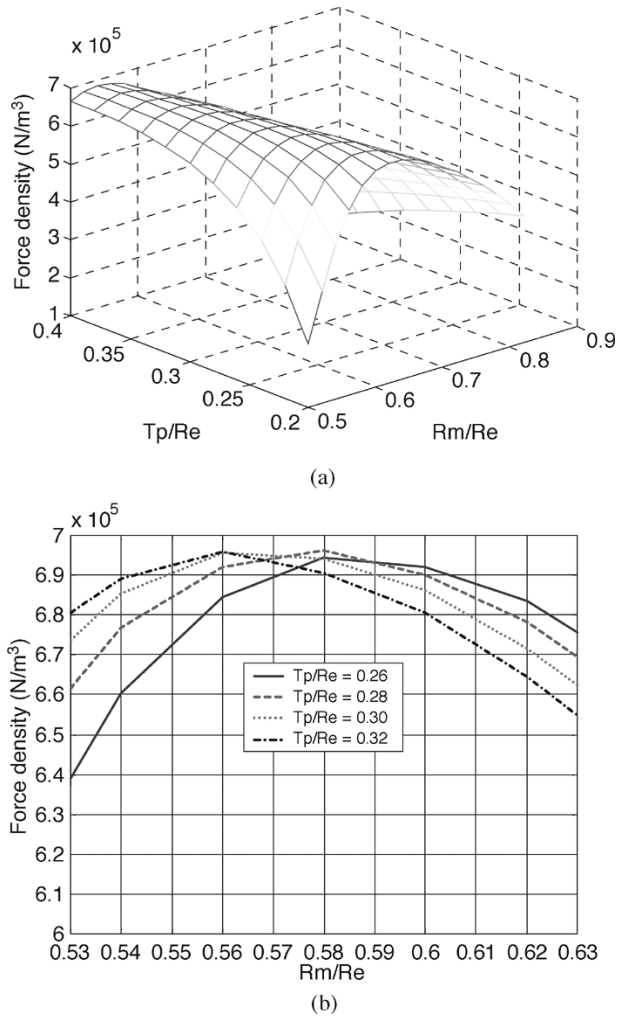

Fig. 15. Variation of force density with R_m/R_e and τ_p/R_e. (a) 3-D view. (b) 2-D view.

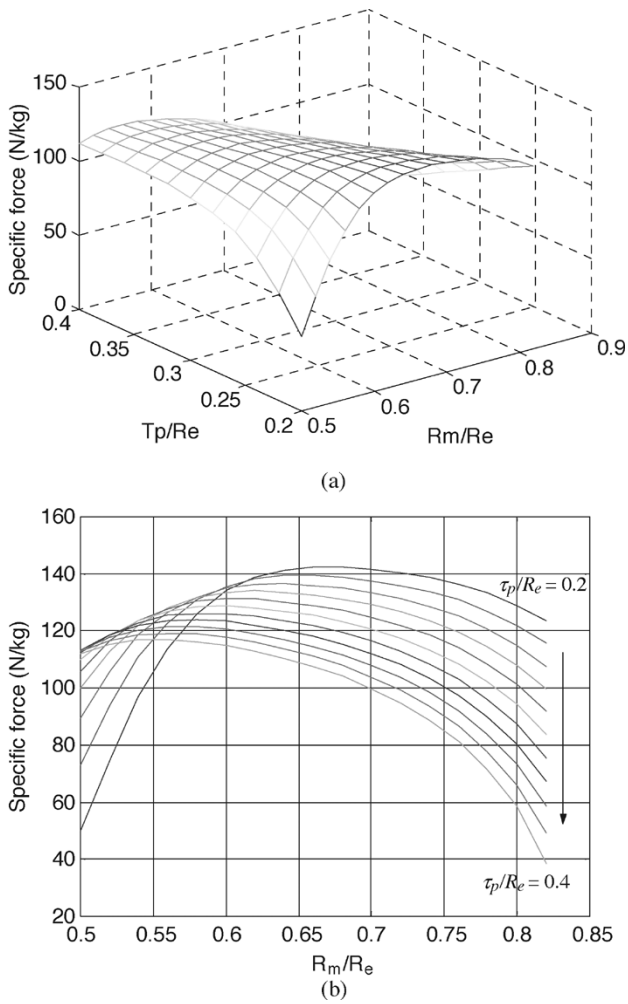

Fig. 16. Variation of specific force with R_m/R_e and τ_p/R_e. (a) 3-D view. (b) 2-D view.

TABLE III
FIXED DESIGN PARAMETERS OF TUBULAR PERMANENT-MAGNET MACHINE

h_m (m)	G (m)	R_e (m)	b_0 (m)	τ_m/τ_p	k_θ (W/m^2/K)	ΔT (C^0)
0.005	0.001	0.1	0.004	1.0	195	120

imum permissible flux density in the cores. In order that the findings are independent of machine size, the thrust force due to the fundamental component of the radial air-gap field is divided by the volume of the stator, $\pi R_e^2 l_e$, to give the force density (i.e., force per unit volume). In many applications, multiple design objectives are often sought, for example, to maximize the force density or efficiency for minimum cost, and the criteria that are used to judge an optimal design may vary from one application to another. In order that the findings are generic, therefore, the subsequent study focuses on the influence of leading design parameters on key cost and performance indicators, such as force/power density, specific force/power, efficiency, and power factor, rather than on a specific objective.

For a given outer radius R_e, the design parameters that have a significant influence on the performance are the dimensional ratios R_m/R_e, τ_p/R_e, τ_m/τ_p, the magnet thickness h_m, and the air-gap length G. In general, the performance improves as h_m is increased. However, an increase in the volume of rare-earth magnet material will increase the cost and result in a heavier armature, which is usually undesirable for a moving-magnet machine. In this study, therefore, the magnet thickness is fixed (at 5 mm) to produce an acceptable air-gap flux density and force density, while providing the required demagnetization withstand capability. The air-gap length G is also assumed to be constant (at 1 mm), since although a smaller air-gap length would also improve the performance, it is limited by manufacturing tolerances, and the stiffness and static and dynamic radial run-out of the moving armature. The influence of τ_m/τ_p on the performance and cost is also straightforward. Both the force density and efficiency increase as the ratio τ_m/τ_p is increased, but the volume of rare-earth magnet material and, hence, the cost will also increase. However, there is an optimal ratio of τ_m/τ_p for minimum harmonic distortion in the air-gap field distribution and force ripple [18]. This optimal ratio is around 0.8, although it may vary slightly with different machine designs.

Fig. 15 shows the variation of the force density as a function of R_m/R_e and τ_p/R_e assuming that the magnets have a remanence $B_{\rm rem} = 1.04$ (T) and a relative recoil permeability $\mu_r = 1.05$ for the calculation of the open-circuit magnetic field,

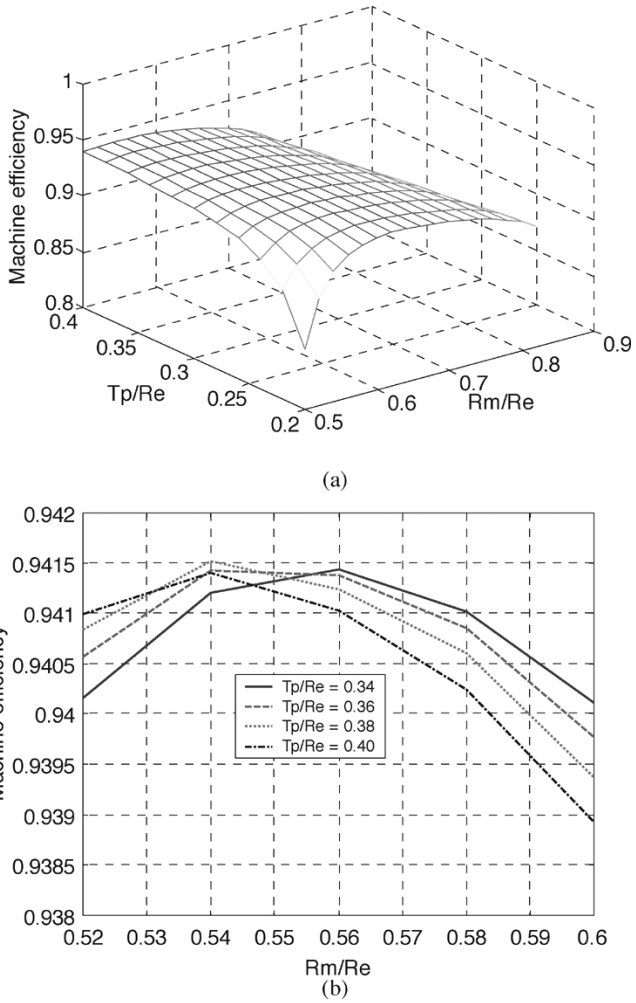

Fig. 17. Variation of machine efficiency with R_m/R_e and τ_p/R_e. (a) 3-D view. (b) 2-D view.

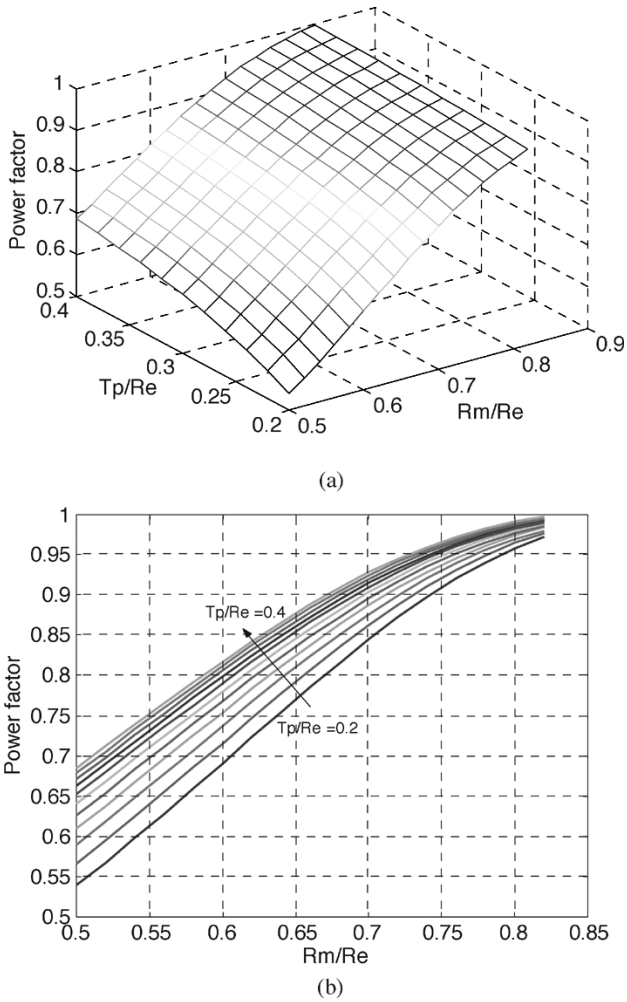

Fig. 18. Variation of power factor with R_m/R_e and τ_p/R_e. (a) 3-D view. (b) 2-D view.

and a value $\mu_r = 1.0$ for the calculation of the armature reaction field, and that the coils have a packing factor $k_{pf} = 0.5$. The other design parameters and thermal constraints are given in Table III. As will be seen, for a given τ_p/R_e, there is an optimal ratio of R_m/R_e which yields the maximum force density. This ratio represents an optimal balance between the electric loading and the magnetic loading of the machine for a given thermal performance. Similarly, for a given R_m/R_e, an optimum value of τ_p/R_s exists, which results in the maximum force density. As the ratio of τ_p/R_e is reduced below the optimum value, the air-gap field that is produced by the permanent magnets decays more rapidly with radius and interpole flux leakage increases. Hence, the force capability reduces. However, if the ratio of τ_p/R_e is too large, the flux per pole increases and this results in increased saturation of both the stator and armature cores if their radii are maintained constant, or requires thicker cores if their flux density is to be maintained constant. In both cases, the force density again reduces. The optimal dimensional ratios for the maximum force density of 696.3 kN/m^3 are $R_m/R_e = 0.58$ and $\tau_p/R_e = 0.28$.

Fig. 16 shows the variation of the specific force (i.e., force per unit mass) as a function of the dimensional ratios R_m/R_e and τ_p/R_e. A similar trend is observed, in that for a given ratio τ_p/R_e there exists an optimal value of R_m/R_e, which yields the maximum specific force. However, this optimal ratio increases as τ_p/R_e decreases. This is due to the fact that, for a given outer radius R_e and pole-pitch τ_p, the total weight of the machine reduces as the ratio R_m/R_e is increased.

Figs. 17 and 18, respectively, show the variation of the machine efficiency and power factor as functions of the two-dimensional ratios R_m/R_e and τ_p/R_e. As will be seen, optimal ratios of $R_m/R_e = 0.54$ and $\tau_p/R_e = 0.38$ exist, which yield the maximum machine efficiency of 0.942. This trend is similar to that which was observed in Fig. 15, although the optima occur at slightly different dimensional ratios. It should be noted that the power factor increases as both ratios are increased. This is due to the fact that the slot leakage accounts for a large portion of the machine inductance, and it decreases as the slot depth is reduced with an increase in R_m and as the slot width is increased with an increase in τ_p.

In order to illustrate how the power factor might affect the outcome of the design optimization, Fig. 19 shows the variation of the machine efficiency, the drive system efficiency, the power factor, and the VA rating of the converter as a function of R_m/R_e for a fixed τ_p/R_e ratio of 0.25 and a constant power output of 44 kW. The parameters for evaluation of converter

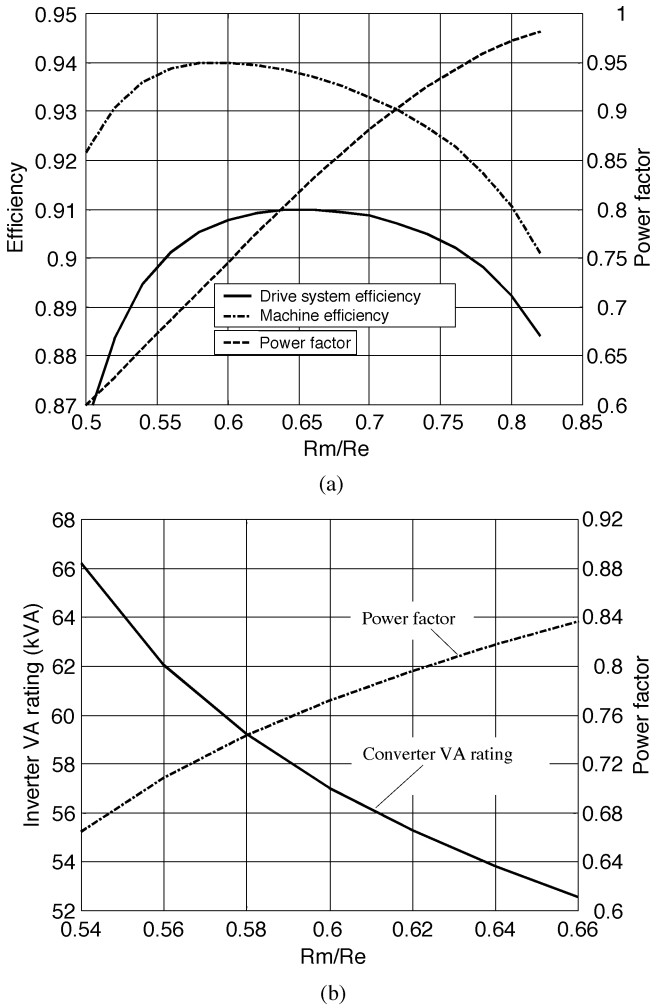

Fig. 19. Variation of machine and drive efficiency, converter VA rating and power factor with R_m/R_e. (a) Efficiency and power factor. (b) VA rating and power factor.

TABLE IV
PARAMETERS FOR EVALUATION OF CONVERTER LOSSES

V_{ton} (V)	R_{ton} (mΩ)	V_{don} (V)	R_{don} (mΩ)	f_s (kHz)
1.0	5.0	1.3	0.3	8.0
I_{cn} (A)	Q_{rrn} (μC)	t_{rrn} (ns)	t_{rr} (ns)	t_{fn} (ns)
300	3.9	450	351	335

losses are given in Table IV. As will be seen, the optimal R_m/R_e ratio of 0.59 for the maximum machine efficiency is much lower than the ratio of 0.66 for maximum drive system efficiency. This is because at the optimal ratio for maximum machine efficiency, the power factor is much lower, and, hence, the converter loss is higher. As the ratio R_m/R_e is increased, the converter efficiency initially increases faster than the decrease in the machine efficiency and the drive system efficiency improves until a point is reached where this trend reverses. It should also be noted that the required converter VA rating at $R_m/R_e = 0.59$ is significantly higher than that which is required for the maximum drive system efficiency. Thus, machine design optimization without taking account of the converter loss and VA rating may not only lead to a less efficient system but also a higher cost.

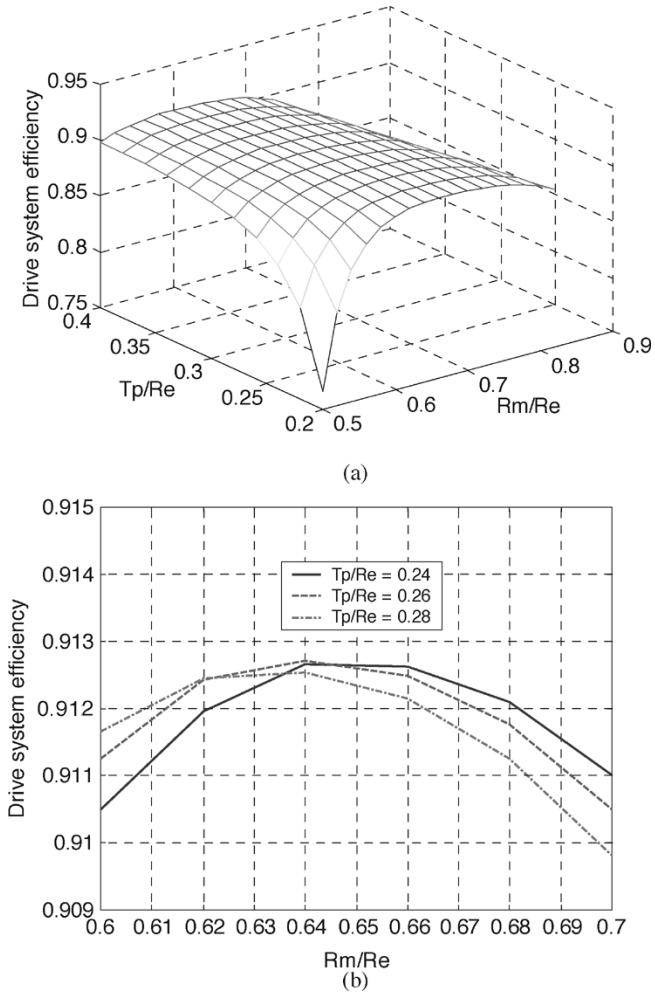

Fig. 20. Variation of drive system efficiency with R_m/R_e and τ_p/R_e. (a) 3-D view. (b) 2-D view.

Fig. 20 shows the variation of the drive system efficiency as a function of the two-dimensional ratios R_m/R_e and τ_p/R_e. As will be seen, optimal ratios of $R_m/R_e = 0.64$ and $\tau_p/R_e = 0.26$ also exist, which yield the maximum drive system efficiency of 0.9127. However, these are quite different from those in Fig. 17 in which only the machine efficiency is considered. As has been shown in Fig. 18, the power factor of the machine improves as R_m/R_e increases. As a result, the optimal ratio of R_m/R_e for different values of τ_p/R_e and maximum drive system efficiency tends to be greater than 0.58. As can be seen in Fig. 17(b), in the region where R_m/R_e is greater than 0.58, the machine efficiency increases as the ratio τ_p/R_e decreases. Thus, although a decrease in τ_p/R_e results in a reduction in power factor, which tends to reduce the drive system efficiency, this reduction is outweighed by the increases in the machine efficiency. Consequently, the optimal ratio of τ_p/R_e for maximum drive system efficiency is much lower than that for maximum machine efficiency.

IX. CONCLUSION

Analytical formulas for predicting the parameters and performance of radially magnetized, iron-cored, tubular permanent-

magnet machines and drive systems, with due account of magnetic saturation and subject to a specific thermal constraints, have been established. Their utility and accuracy have been validated by finite-element analysis. The derived formulas provide an effective means of optimizing the design of machines and drive systems, and will aid the design process when addressing a given performance specification. It has been shown that for a converter-fed drive system, the power factor has a significant influence on the system efficiency and cost, and, as such, it is essential that the converter losses and its VA rating are taken into account during the design optimization of the permanent-magnet machine.

APPENDIX

Definition of a_{an} and b_{an}

Let:

$$c_{1n} = BI_0(m_{an}R_0); \quad c_{2n} = BK_0(m_{an}R_0)$$
$$c_{3n} = BI_0(m_{an}R_{se}); \quad c_{4n} = BK_0(m_{an}R_{se})$$
$$\Delta_n = c_{2n}c_{3n} - c_{1n}c_{4n}; \quad d_n = \frac{2\mu_0 N_c I}{\tau_p} K_{dan} K_{pan}$$
$$a_{an} = \frac{c_{2n}d_n}{\Delta_n}; \quad b_{an} = \frac{c_{1n}d_n}{\Delta_n}.$$

REFERENCES

[1] J. F. Eastham, "Novel synchronous machines: linear and disc," *Proc. Inst. Elect. Eng.*, vol. B-137, pp. 49–58, 1990.

[2] E. Masada, "Linear drives for industrial applications in Japan—history, existing state and future prospect," in *Proc. LDIA'95*, Japan, 1995, pp. 9–12.

[3] M. A. White, K. Colenbrander, R. W. Olan, and L. B. Penswick, "Generators that won't wear out," *Mech. Eng.*, vol. 118, no. 2, pp. 92–96, 1996.

[4] W. R. Cawthorne, P. Famouri, J. Chen, N. N. Clarke, T. I. McDaniel, R. J. Atkinson, S. Nandkumar, C. M. Atkinson, and S. Petreanu, "Development of a linear alternator-engine for hybrid electric vehicle applications," *IEEE Trans. Veh. Technol.*, vol. 48, no. 6, pp. 1797–1802, 1999.

[5] R. E. Clark, D. S. Smith, P. H. Mellor, and D. Howe, "Design optimization of moving-magnet actuators for reciprocating electro-mechanical systems," *IEEE Trans. Magn.*, vol. 31, pp. 3746–3748, Nov. 1995.

[6] M. Watada, K. Yanashima, Y. Oishi, and D. Ebihara, "Improvement on characteristics of linear oscillatory actuator for artificial hearts," *IEEE Trans. Magn.*, vol. 29, pp. 3361–3363, Nov. 1993.

[7] K. Park, E. P. Hong, and K. H. Lee, "Development of a linear motor for compressors of household refrigerators," in *Proc. LDIA'2001*, Japan, pp. 283–286.

[8] M. Utsuno, M. Takai, T. Yaegashi, T. Mizuno, H. Yamamoto, K. Shibuya, and H. Yamada, "Efficiency Characteristics of a linear oscillatory actuator under simulated compressor load," in *Proc. LDIA'2001*, Japan, pp. 264–267.

[9] I. Boldea and S. A. Nasar, *Linear Electric Actuators and Generators*. Cambridge, U.K.: Cambridge Univ. Press, 1997.

[10] T. Mizuno and H. Yamada, "Magnetic circuit analysis of a linear synchronous motor with permanent magnets," *IEEE Trans. Magn.*, vol. 28, pp. 3027–3029, Sept. 1992.

[11] R. Akmese and J. F. Eastham, "Dynamic performance of a brushless DC tubular drive system," *IEEE Trans. Magn.*, vol. 25, pp. 3269–3271, Sept. 1989.

[12] J. F. Eastham, R. Akmes, and H. C. Lai, "Optimum design of brushless tubular linear machines," *IEEE Trans. Magn.*, vol. 26, pp. 2547–2549, Sept. 1990.

[13] A. Basak and G. H. Shirkoohi, "Computation of magnetic field in D.C. brushless linear motors built with NdFeB magnets," *IEEE Trans. Magn.*, vol. 26, pp. 948–950, Mar. 1990.

[14] G. Xiong and S. A. Nasar, "Analysis of fields and forces in a permanent magnet linear synchronous machine based on the concept of magnetic charge," *IEEE Trans. Magn.*, vol. 25, pp. 2713–2719, May 1989.

[15] Z. J. Liu, A. Vourdas, and K. J. Binns, "Magnetic field and eddy current losses in linear and rotating permanent magnet machines with a large number of poles," *Proc. Inst. Elect. Eng.*, vol. A-138, no. 6, pp. 289–294, 1991.

[16] D. L. Trumper, W. Kim, and M. E. Williams, "Design and analysis framework for linear permanent magnet machines," *IEEE Trans. Ind. Applicat.*, vol. 32, pp. 371–379, Mar./Apr. 1996.

[17] J. Wang, G. W. Jewell, and D. Howe, "A general framework for the analysis and design of tubular linear permanent magnet machines," *IEEE Trans. Magn.*, vol. 35, pp. 1986–2000, May 1999.

[18] ——, "Design optimization and comparison of tubular permanent magnet machine topologies," *Proc. Inst. Elect. Eng.—Electric Power Applications*, vol. 148, no. 5, pp. 456–464, 2001.

[19] Q. Gu and H. Gao, "Effect of slotting in PM electrical machines," *Elect. Mach. Power Syst.*, vol. 10, no. 2, pp. 273–284, 1985.

[20] Z. Q. Zhu and D. Howe, "Instantaneous magnetic field distribution in brushless permanent magnet dc motors—part III: effect of stator slotting," *IEEE Trans. Magn.*, vol. 29, pp. 143–151, Jan. 1993.

[21] K. Atallah, Z. Q. Zhu, and D. Howe, "The prediction of iron losses in brushless permanent magnet dc motors," in *Proc. Int. Conf. Electrical Machines*, 1992, pp. 814–818.

[22] Z. Q. Zhu and D. Howe, "Instantaneous magnetic field distribution in brushless permanent magnet dc motors—part II: armature reaction field," *IEEE Trans. Magn.*, vol. 29, pp. 136–142, Jan. 1993.

[23] L. K. Mestha and P. D. Evans, "Analysis of on-state losses in PWM inverters," *Proc. Inst. Elect. Eng.—Electric Power Applications*, vol. 136, no. 4, 1989.

[24] F. Casanellas, "Losses in PWM inverters using IGBTs," *Proc. Inst. Elect. Eng.—Electric Power Applications*, vol. 141, no. 5, 1994.

Jiabin Wang (M'96–SM'03) was born in Jiangsu Province, China, in 1958. He received the B.Eng. and M.Eng. degrees in electrical engineering from Jiangsu University of Science and Technology, Zhengjiang, China, in 1982 and 1986, respectively, and the Ph.D. degree in electrical and electronic engineering from the University of East London, London, U.K., in 1996.

Currently, he is a Senior Lecturer at the University of Sheffield, Sheffield, U.K. From 1986 to 1991, he worked in the Department of Electrical Engineering, Jiangsu University of Science and Technology, where he was appointed a Lecturer in 1987 and an Associated Professor in 1990. He was a Postdoctoral Research Associate at the University of Sheffield, Sheffield, U.K., from 1996 to 1997 and a Senior Lecturer at the University of East London from 1998 to 2001. His research interests range from motion control to electromagnetic devices and their associated drives.

David Howe received the B.Tech and M.Sc. degrees from the University of Bradford, Bradford, U.K., in 1966 and 1967, respectively, and the Ph.D. degree from the University of Southampton, Southampton, U.K., in 1974, all in electrical power engineering.

Currently, he is a Professor of Electrical Engineering at the University of Sheffield, Sheffield, U.K., where he heads the Electrical Machines and Drives Research Group. He has held academic posts at Brunel University, London, U.K., and Southampton University, and spent a period in industry with NEI Parsons Ltd, Newcastle-Upon-Tyne, U.K., working on electromagnetic problems related to turbo-generators. His research activities span all facets of controlled electrical drive systems, with particular emphasis on permanent-magnet excited machines.

Professor Howe is a Chartered Engineer, a Fellow of the IEE, U.K., and a Fellow of the Royal Academy of Engineering, U.K.